A fully generalised approach to modelling fire response of steel–RC composite structures

J. Kolšek [a], M. Saje [b,*], I. Planinc [b], T. Hozjan [b]

[a] ZAG - Slovenian National Building and Civil Engineering Institute, Fire Laboratory, Dimičeva 12, SI-1000 Ljubljana, Slovenia
[b] University of Ljubljana, Faculty of Civil and Geodetic Engineering, Chair of Mechanics, Jamova 2, SI-1115 Ljubljana, Slovenia

A R T I C L E   I N F O

A B S T R A C T

A three-step model for the performance-based numerical simulations of the fire response of steel–RC two-layered beam-like composite structures is presented and validated. The first step consists of the determination of the evolution of temperatures in the structure's surroundings. Moisture and the heat transfer through the RC layer and the conduction of heat over the steel layer are obtained in the second step. In concrete, the transfer of water vapour, dry air, and free water is discussed as well as the evaporation and liquefaction phenomena and the dehydration of concrete and its thermal and mechanical degradation. Within the framework of the third step, a geometrically and materially non-linear mechanical response of the structure is proposed accounting for interlayer slips and uplifts as well as for various material-related phenomena such as the material hardening/softening and creep. The governing equations are solved numerically. An efficient, novel strain-based finite element formulation is introduced for the mechanical analysis. Due to its generality and consideration of several different possible non-linear material, geometrical, and interlayer contact phenomena and their couplings the model can be of a use to a broader fire science community for exploring the impact of different physical parameters on the results of the addressed numerical simulations, thereby providing directions for further research. In the paper a case of such a study is also demonstrated exploring the contribution of the steel sheet and the flexibility of the interlayer connection of a standard trapezoidal steel–RC slab to its ultimate fire resistance. A reasonable contribution of the sheet is proved if the stiffness ratio between the integrated and the external tensile reinforcement of the RC plate is low provided that the contact connection is sufficiently stiff.

1. Introduction

In structural fire engineering, the so-called 'performance-based design' approach has become the highly popular issue in recent years. This novel approach enables us to predict the overall structural fire response much more realistically than the traditional 'prescriptive-based' one, thus providing a better reliability of the corresponding designed fire safety measures and their cost efficiency. In the last couple of decades, significant amount of scientific work has been put into development of suitable procedures for such a design. Nevertheless, a vast amount of problems still remains insufficiently understood and a matter of intense ongoing further investigation. Part of these are also performance-based procedures for fire response of steel–RC composite beam-like structures.

The problem of the fire response of a steel–RC two-layered beam-like structure is complex from different perspectives. Most of these originate from high-temperature material behaviour (especially those of porous concrete) and contact interactions (i.e. effect of the flexibility and bearing capacity of the contact connection between the steel and the RC layer). Connected to considerations of contact interactions the review of the scientific literature has shown that the contribution of the steel layer to the overall structural fire performance is, in the performance-based fire design procedures, frequently neglected. Instead, the standard numerical models for RC structures ignoring the layered nature of the beam are applied. These models are especially adopted when the steel layer appears in a form of a thin sheet and is unprotected against fire, which is the case with the externally strengthened RC structures such as tension face-plated, side-plated RC beams or classic trapezoidal steel–RC floor slabs. Although omitting the layer of a thin steel sheet from the numerical simulation may seem to be reasonable at first glance, it could result in a substantial underestimation of the actual structural fire resistance in some cases [1]. Additionally, potentially life-threatening events, such as

* Corresponding author. Tel.: +386 1 47 68 613; fax: +386 1 42 50 681.
E-mail address: miran.saje@fgg.uni-lj.si (M. Saje).

a sudden premature de-bonding (peel off) of the overheated steel strengthening layer at unsupported edges, could be overlooked. To avoid such unfortunate modelling uncertainties as much as possible, numerical models accounting for both the RC and the steel layers should be adopted. Only a few such models have been presented so far (e.g. [1–3]). They are, however, still not sufficiently generalised to describe the behaviour of an arbitrary composite beam in fire. Their common assumption is that the interlayer connection is only deformable in the tangential direction, while the contact in the normal direction is taken to be rigid (e.g. [3,4]). In an ambient temperature structural analysis, a significant error may result from such an assumption, as analyses have already shown [5] and a pronounced effect could be also expected for high temperature conditions. In [5], the normal contact stiffness between the layers of a steel–RC composite beam is reported to significantly influence the beam shear forces, which does not always act in favour of the beam. In addition, although not so clear a priori, a substantial effect of slips and uplifts between the layers is also detected. It is therefore concluded that the effect of the flexibility of the interlayer connection both in the tangential and in the normal direction should not be disregarded in the design process.

The second important source of the high complexity of the problem of steel–RC composite structures in fire, however, is the material models, especially those of concrete. Concrete is a highly heterogeneous multi-phase material and consists of the solid matrix representing the hardened cement paste and aggregates as well as of pores. These are filled with water (liquid, adsorbed or chemically bound), dry air, and water vapour. Due to the presence of pressurised fluids and their concentration gradients (these are generated as a result of phase changes, i.e. water evaporation and vapour condensation) and concrete permeability gradients, mass fluxes of water and gas inside the pores emerge during fire. Consequently, the heat is not only conducted but also convected through the material what influences the evolution of the temperature in concrete [1,2]. In addition, on account of the physical and chemical decomposition of concrete, and of the stress, induced by either external mechanical loads or by the restrained thermal dilatations, substantial cracking occurs as well. Such concrete damage results in the deterioration of the mechanical moduli of concrete and the increase of its permeability. Combined with a sufficiently high pore pressures, damage of concrete eventually results in concrete spalling [6–8] and jeopardises the overall structural integrity. In recent years several numerical models were proposed trying to simulate these complex phenomena. The first group of these models (e.g., [9–11]) called the multi-step models with uncoupled hygro-thermal and mechanical analyses is applicable if zero or negligibly small mechanical loading is applied and where thermal dilatations of the concrete element are not significantly restrained, so that only small stress is induced in the element during fire. In lieu of these models, although at date still a matter of intense ongoing research and validation studies, some modelling proposals are also already available for more general cases of arbitrary loaded concrete structures. In these the hygro-thermal and mechanical phenomena are coupled fully [7,8], or, they are connected indirectly [12,6].

In this paper the recent improvements in concrete hygro-thermal constitutive models [11,12,6] and description of contact interaction between the layers of two-layered composite structures [5,13] are brought together with the authors' previous work on composite structures in fire. Then, the joint modelling principles are exploited for the evolution and validation of a novel numerical model for performance-based simulations of fire response of an arbitrary steel–concrete composite beam-like structure. The new model is generalised in the sense that it gathers submodels for all phenomena (highly non-linear material,

geometrical, and contact interlayer high-temperature responses) and their couplings that are at date recognised as potentially influential for the addressed problem. As such, the model can be of a good use to a broader fire research community for performing extended parametric studies, i.e. studies exploring importance of specific physical phenomena for efficiency and accuracy of the numerical simulations. In this way the model also enables detection of the phenomena that can or cannot be neglected in the models or accounted for in a simplified manner. An example of such a study is presented in the final part of the paper. This shows a parametric study investigating the contribution of the thin steel sheet and of the stiffness of the steel sheet–RC contact connection to the overall structural fire resistance of a standard trapezoidal steel–RC floor slab.

2. The fire analysis of a steel–RC beam-like structure

2.1. Preliminaries

Consider a planar straight RC beam 'a' of length L^a connected to a steel layer 'b' of length L^b where $L^a = L^b = L$. The layers have constant, yet arbitrary cross-sections, $\mathcal{A}_x^a$ and $\mathcal{A}_x^b$ (Fig. 1). They are connected either with discrete connectors (e.g. bolts) or continuously with an adhesive bonding layer of small thickness. As this connection is not perfectly rigid in either of the two cases, the longitudinal (here called the tangential) slips and the transversal (here called the normal) uplifts can occur between the layers during deformation. We assume that, at a specific time instant, the mechanically loaded observed structure is suddenly exposed to fire loads causing it to deform significantly until it collapses. We call the time of collapse of the structure its fire resistance. To pursue deforming of the structure during fire and to obtain its ultimate fire resistance, a three-step numerical procedure is proposed later in the section.

2.2. The model

2.2.1. The first step of the analysis: the fire compartment temperature analysis
In the first step of the proposed fire analysis, the time evolution of the gas temperature in the compartment, surrounding the structure, needs firstly be defined. As the prime interest of the present paper is to investigate effects of fire on the thermo-mechanical state within the structure, the standard ISO834 fire curve [14] suffices to be selected for these purposes.

2.2.2. The second step of the analysis: the hygro-thermal analysis
In the second step of the fire analysis, we observe the hygro-thermal response of the structure. The heat transfer in the homogeneous non-porous steel layer is modelled by standard Fourier's law of heat conduction. In contrast, the model of heat transfer in concrete, which is a heterogeneous material consisting also of pores, filled with water, water vapour and dry air, should additionally consider transfer of moisture. One of the models well appropriate for the analysis of concrete-like heterogeneous materials is the model of Davie et al. [11]. The model accounts for evaporation of free water, liquefaction of water vapour, and dehydration of the chemically bound water, and comprises the following three equations of the mass conservation of free water, water vapour and dry air:

$$\frac{\partial(\varepsilon_{FW}\rho_{FW})}{\partial t} = -\nabla \cdot \mathbf{J}_{FW} - \dot{E}_{FW} + \frac{\partial(\varepsilon_D\rho_{FW})}{\partial t}, \tag{1}$$

$$\frac{\partial(\varepsilon_G\tilde{\rho}_V)}{\partial t} = -\nabla \cdot \mathbf{J}_V - \dot{E}_{FW}, \tag{2}$$

$$\frac{\partial(\varepsilon_G \tilde{\rho}_A)}{\partial t} = -\nabla \cdot \mathbf{J}_A, \tag{3}$$

and the equation of the energy conservation:

$$(\underline{\rho c})\frac{\partial T}{\partial t} = -\nabla \cdot (-k\nabla T) - (\underline{\rho c \mathbf{v}}) \cdot \nabla T - \lambda_E \dot{E}_{FW} - \lambda_D \frac{\partial(\varepsilon_D \rho_{FW})}{\partial t}. \tag{4}$$

In Eqs. (1)–(4) $\varepsilon_i \rho_i$ represents the mass concentration of phase i (index i applies to phases of concrete: FW is free water, V is water vapour and A is dry air), $\tilde{\rho}_i$ represents the mass of phase i per unit volume of gaseous material ($i = V, A$) and $\dot{E}_{FW}$ is the time rate of evaporation of free water (including desorption). Furthermore, t applies to time, ρc is the heat capacity of concrete, k is its thermal conductivity, and $\underline{\rho c \mathbf{v}}$ is the energy transferred by fluid flow. The latter can be neglected, if the thermal conductivity coefficient of concrete, k, is substituted by the corresponding value for moist concrete, as, e.g. is advised in EC2 [15], and also adopted in this paper. λ_E and λ_D, respectively, apply to specific heat of evaporation and dehydration, T stands for the temperature, and $\mathbf{J}_i$ denotes the mass flux of phase i. The mass fluxes $\mathbf{J}_i$ are to be expressed in terms of pressure and concentration gradients implementing standard Darcy's and Fick's laws. These and the rest of the constitutive equations, adopted in the proposed hygro-thermal submodel, are to be applied according to [11]. Nevertheless, an exception is to be made regarding the calculations of time-dependent concrete permeability representing the basic variable of Darcy's law. According to the nature of the problem discussed in the case study of Davie et al. [11], zero 'mechanical' (i.e. stress induced) effects are assumed in the determination of the increase in concrete permeability and pressure-driven fluid flows with time. The submodel [9] for the evolution of concrete permeability in time is implemented correspondingly. Nevertheless, for a general case of an externally strengthened RC beam exposed to fire, the stress induced effects are pronounced for majority of cases and they need to be considered explicitly. One such a proposal was introduced by Dwaikat and Kodur [6,12] and their permeability submodel is adopted in the present paper.

According to Dwaikat and Kodur [2], in a pure hygro-thermal model (such as the model by Davie et al. [11]) the permeability of concrete is to be calculated by accounting for the gradients in the initial permeability of concrete:

$$K_0 = K_{top}\begin{cases} 10^{2y/h}, & y \le d_{neu} \\ (10^{2y/h})(10^{3(y-d_{neu})/(h-d_{neu})}), & y > d_{neu} \end{cases}. \tag{5}$$

In Eq. (5) K_{top} is the initial permeability in the top surface of the RC section, h denotes the depth of the concrete cross-section, y is the distance from top of the cross-section, and d_{neu} is the depth of the neutral axis at service loads and ambient temperature. Furthermore, at each time station $t > 0$, the permeability of concrete, K, is changed additionally considering the current temperature of concrete, T, and the averaged pressure of liquids and gas inside the solid concrete matrix (i.e. pore pressure), P_{pore} [2,3]:

$$K(T) = K_0\left[10^{0.0025(T-T_0)}\left(\frac{P_{pore}}{P_0}\right)^{0.368}\right]. \tag{6}$$

Note that the above proposals, i.e. Eqs. (5) and (6), were designed specifically for the evaluations of concrete permeability in flexural RC beams.

A further advantage of the proposal of Dwaikat and Kodur [12,6] is that, simultaneously, the fire induced concrete spalling (if any) can be pursued as well implementing the criterion [2]:

$$p_{or} \cdot P_{pore} > f_{ct,T}. \tag{7}$$

In Eq. (7) $f_{ct,T}$ is the tensile strength of concrete and p_{or} is the porosity defined as the fraction of the volume of voids over the total volume of the material and for high temperatures calculated as proposed in [11]. According to this criterion, spalling is said to occur when the effective pore pressure exceeds the temperature dependent tensile strength of concrete.

Note that because concrete spalling is not considered to be a noticeable problem in practical examples shown throughout the present paper, where only structures involving normal strength concrete layers are presented, this topic will not be discussed further in the sequel. Note also that the problem of concrete spalling is at present date in the broader scientific community still not understood sufficiently, mostly because the physical phenomena involved in this complex process are hard to measure experimentally. Thus, the available models dealing with this complex problem

Fig. 1. The two-layered composite beam. Undeformed and deformed configurations.

(including the one implemented here) are still a mater of further ongoing investigation.

To obtain the numerical solution of the presented equations of the hygro-thermal submodel, a standard Galerkin-type of the finite element method is employed as proposed in [11]. Once the solution has been obtained, the data showing temperatures and, yet only for cases of pronounced pore pressures and concrete spalling, pore pressures and the spalled concrete areas are employed as the input for the final, mechanical part of the fire analysis.

2.2.3. The third step of the analysis: the mechanical analysis

The objective of the mechanical analysis is to compute the stress–strain state evolution in the composite beam during fire. The numerical model presented in this paper originates from a recent work of the authors and their co-workers on the composite structures in general and on fire safety engineering in particular. Hence, solely the fundamental novelties of the proposed model will here be presented in detail and adequate references will be given where appropriate.

The (X,Z)-plane of a fixed spatial right-handed Cartesian coordinate system (X, Y, Z) with the orthonormal base vectors $\mathbf{E}_X$, $\mathbf{E}_Z$, and $\mathbf{E}_Y = \mathbf{E}_Z \times \mathbf{E}_X$ and with the origin pinned at an arbitrary fixed reference point O is chosen as the plane of the possible deformation of the structure (Fig. 1). In addition to the global coordinate system, each layer is also parametrised by its own material coordinate system (x^i, y^i, z^i), $i = a$ or b with the axis x^i declared as the layer's reference axis. The material coordinate system is defined by its origin O^i and its orthonormal vectors $\mathbf{e}_t^i$, $\mathbf{e}_m^i$, and $\mathbf{e}_n^i$, being tangential, out-of-plane and normal to the deformed axis of the beam, respectively. The basic feature of the material coordinate system is that its coordinate axes follow the deformation of the layer and that, therefore, material coordinates of a particular particle do not change during the deformation. Furthermore, we define that, in the initial undeformed state, the positions of both reference axes x^a and x^b, respectively, of layers a and b coincide and that they both lie on the vertical symmetry plane of the beam; note, however, that an arbitrary initial position of the origin relative to the height of the beam can be chosen. If we further decide that, in the undeformed state, the material axes coincide also with the spatial axes, we have $x^a \equiv x^b \equiv X \equiv x$, $y^a \equiv y^b \equiv Y \equiv y$, and $z^a \equiv z^b \equiv Z \equiv z$. Once the position of an individual particle as well as its thermo-mechanical fields is described in terms of the material coordinates, the Lagrangian description of the solid body deformation can be employed for the purposes of the model derivation.

In what follows, each of the two layers of the observed steel–RC composite beam will be modelled separately, assuming the geometrically exact planar beam theory of Reissner [17] with negligible effects of shear deformations. The related governing equations of layer 'i' ($i = a, b$) are

$$1 + u^{i'} - (1 + \varepsilon^i) \cos \varphi^i = 0, \tag{8}$$

$$w^{i'} + (1 + \varepsilon^i) \sin \varphi^i = 0, \tag{9}$$

$$\varphi^{i'} - \kappa^i = 0, \tag{10}$$

$$R_X^{i'} + \mathcal{P}_x^i = 0, \tag{11}$$

$$R_Z^{i'} + \mathcal{P}_z^i = 0, \tag{12}$$

$$M^{i'} - (1 + \varepsilon^i) Q^i + \mathcal{M}_y^i = 0, \tag{13}$$

$$N_{eff}^i = N^i + N_{pore}^i = \int_{\mathcal{A}_x^i} \sigma^i(D_\sigma^i, T) \, dA_x^i + N_{pore}^i, \tag{14}$$

$$M_{eff}^i = M^i + M_{pore}^i = \int_{\mathcal{A}_x^i} z^i \sigma^i(D_\sigma^i, T) \, dA_x^i + M_{pore}^i. \tag{15}$$

In Eqs. (8)–(15) $(\bullet)'$ denotes the derivative with respect to material coordinate x, u^i, w^i, and φ^i, respectively, apply to the X-displacement, the Z-displacement and the rotation of the reference axis of layer i, and ε^i and κ^i denote its extensional and bending strains, respectively. Furthermore, R_X^i and R_Z^i are, respectively, the X and the Z components of the cross-sectional stress-resultant with respect to the fixed basis ($\mathbf{E}_X$, $\mathbf{E}_Y$, $\mathbf{E}_Z$), and N^i, Q^i, and M^i are, respectively, the cross-sectional axial force, shear force, and bending moment. Note that R_X^i and R_Z^i relate to N^i and Q^i as follows: $N^i = R_X^i \cos \varphi^i - R_Z^i \sin \varphi^i$ and $Q^i = R_X^i \sin \varphi^i + R_Z^i \cos \varphi^i$. $\mathcal{A}_x^i$ is the area of the cross-section of layer 'i' and dA_x^i is its differential. Note that the area of the concrete portion of the cross-section varies with time due to cracking, and, in some cases, due to concrete spalling. In fact, when concrete spalling is detected during the analysis, which often occurs in high-strength wet concrete structures, the area of the RC layer $\mathcal{A}_x^i$ has to be reduced accordingly (see, e.g. [1]). In Eqs. (14) and (15), σ^i and D_σ^i are, respectively, the stress and the mechanical strain of a generic particle of layer 'i', and the relationship $\sigma^i(D_\sigma^i, T)$ is the material constitutive law of concrete/steel at elevated temperatures. The latter is in the present paper taken from standards [15] (for concrete) and [18] or [19] (for steel) with additionally accounting for elastic reloading and kinematic hardening of cyclically loaded and reloaded material [20]. In obtaining strain increments, we assume that the principle of additivity of strains holds [3,1,21]. This enables us to define each type of strain separately. Unconstrained temperature strains of concrete and steel are obtained from formulae in [15,18]. As recommended in [22], creep strain of steel should be accounted for separately if the model proposed by [19] for the constitutive relationship $\sigma^i(D_\sigma^i)$ of steel is selected. By contrast, if the material law for steel is adopted in terms of [18], the creep strain should be an integral part of plastic strain. Finally, if we implement the EC2 constitutive law of concrete [15], the creep and the transient deformations of concrete have to be considered as separate items in the strain additivity principle, as discussed by Bratina et al. [21].

N_{pore}^i and M_{pore}^i, given respectively in Eqs. (14) and (15), represent the contributions of the pore pressures to the total stress of the layer 'i' (the well known Terzaghi's principle). The contributions are zero for a non-porous steel layer. Furthermore, for normal strength RC beam structures, the contribution of N_{pore}^a and M_{pore}^a is very small and can be usually neglected [16]. $\mathcal{P}_X^i$, $\mathcal{P}_Z^i$ and $\mathcal{M}_Y^i$ represent the X, Y, and Z components of the traction vectors per unit of the reference axis of layer 'i', respectively; $\mathcal{P}^i$ and $\mathcal{M}^i$ are the static equivalents of surface and volume forces $\boldsymbol{p}^i$ and $\boldsymbol{v}^i$ (Fig. 1) after having been reduced to the layer's reference axis ($i = a, b$):

$$\mathcal{P}^i = \int_{C_x^i} \boldsymbol{p}^i \, dc_x^i + \int_{\mathcal{A}_x^i} \boldsymbol{v}^i \, dA_x^i = \mathcal{P}_X^i \mathbf{E}_X + \mathcal{P}_Z^i \mathbf{E}_Z, \tag{16}$$

$$\mathcal{M}^i = \int_{C_x^i} \boldsymbol{\rho}^i \times \boldsymbol{p}^i \, dc_x^i + \int_{\mathcal{A}_x^i} \boldsymbol{\rho}^i \times \boldsymbol{v}^i \, dA_x^i = \mathcal{M}_Y^i \mathbf{E}_Y. \tag{17}$$

In Eqs. (16) and (17), C_x^i is the contour of the layer's cross-section (Fig. 1) and dc_x^i is its arc differential. $\boldsymbol{\rho}^i$ is the cross-sectional position vector of a specific particle of layer 'i'. The X-, Y- and Z-components of the traction vectors $\mathcal{P}^i$ and $\mathcal{M}^i$ are made from their external (ex) and contact (cn) contributions: $\mathcal{P}_X^i = \mathcal{P}_{ex,X}^i + \mathcal{P}_{cn,X}^i$, $\mathcal{P}_Z^i = \mathcal{P}_{ex,Z}^i + \mathcal{P}_{cn,Z}^i$, and $\mathcal{M}_Y^i = \mathcal{M}_{ex,Y}^i + \mathcal{M}_{cn,Y}^i$. In the sequel we only discuss the contact traction vectors.

During the deformation of a steel–RC composite beam, the layers can locally slip and/or separate. When large deformations are expected and, consequently, the geometrically non-linear analysis is performed, the slips and uplifts can be large. In such a

case, the contact constitutive equations if written in terms of the global coordinate system ($\mathbf{E}_X$, $\mathbf{E}_Y$, $\mathbf{E}_Z$) are no longer correct [23]. A substantial improvement is reached, if the global coordinate basis is substituted by a 'mean contact surface basis' [13] having the normal and the tangential vectors at the contact as the base vectors $\mathbf{e}_t^*$, $\mathbf{e}_n^*$ and $\mathbf{e}_m^*$ (Fig. 1). The latter are defined as a weighted mean value of the natural basis of layers 'a' and 'b':

$$\mathbf{e}_t^*(x) = \frac{\zeta \mathbf{e}_t^a(x) + (1-\zeta)\mathbf{e}_t^b(x)}{\| \zeta \mathbf{e}_t^a(x) + (1-\zeta)\mathbf{e}_t^b(x) \|} = e_{tX}^*(x)\mathbf{E}_X + e_{tZ}^*(x)\mathbf{E}_Z, \tag{18}$$

$$\mathbf{e}_n^*(x) = \frac{\zeta \mathbf{e}_n^a(x) + (1-\zeta)\mathbf{e}_n^b(x)}{\| \zeta \mathbf{e}_n^a(x) + (1-\zeta)\mathbf{e}_n^b(x) \|} = e_{nX}^*(x)\mathbf{E}_X + e_{nZ}^*(x)\mathbf{E}_Z, \tag{19}$$

$$\mathbf{e}_m^*(x) = \mathbf{e}_n^*(x) \times \mathbf{e}_t^*(x) = (e_{nZ}^*(x)e_{tX}^*(x) - e_{nX}^*(x)e_{tZ}^*(x))\mathbf{E}_Y, \tag{20}$$

where $\| \bullet \|$ is the Euclidean vector norm and $\zeta \in [0,1]$. In this paper, the value $\zeta = 0.5$ will be considered in all the analyses. Note that vectors $\mathbf{e}_n^*$ and $\mathbf{e}_t^*$ cannot always be determined uniquely by the above equations, if $\mathbf{e}_n^a = -\mathbf{e}_n^b$ and $\mathbf{e}_t^a = -\mathbf{e}_t^b$; however, these conditions present no limitations in solving practical problems.

As it will be shown in the sequel, slips and/or uplifts between layers 'a' and 'b' can be presented as the difference of displacements between their deformed configurations. Assume that P^a and P^b are two coincident material points (particles), which, in the undeformed state, stay in contact, hence both at the same position (x, y, z). After deformation of the structure has occurred, their positions with respect to the global coordinate system change and are no longer equal. Their new position vectors are now (Fig. 1)

$$\mathbf{R}^i = X^i\mathbf{E}_X + Y^i\mathbf{E}_Y + Z^i\mathbf{E}_Z, \tag{21}$$

$$X^i = x + U_X^i(x,z), \tag{22}$$

$$Z^i = z + U_Z^i(x,z). \tag{23}$$

Since only in-plane deformations of the structure are dealt with, the Y coordinate of the particle remains unchanged after deformation, i.e. $Y^i = y$. In Eqs. (21)–(23), the spatial coordinates X^i, Y^i, and Z^i depend on the X- and the Z-components U_X^i and U_Z^i of the displacement vector $\mathbf{U}^i = \mathbf{R}^i - \mathbf{R}_0^i$ of the particle in contact (Fig. 1). The 'mean' components, $U_t^{i,*}$ and $U_n^{i,*}$, are related to their spatial components U_X^i and U_Z^i by

$$\mathbf{U}^i = U_X^i(x,z)\mathbf{E}_X + U_Z^i(x,z)\mathbf{E}_Z = U_t^{i,*}(x,z)\mathbf{e}_t^*(x) + U_n^{i,*}(x,z)\mathbf{e}_n^*(x), \tag{24}$$

$$U_X^i(x,z) = u^i(x) + z\,\sin\,\varphi^i(x), \tag{25}$$

$$U_Z^i(x,z) = w^i(x) + z\,\cos\,\varphi^i(x). \tag{26}$$

After the displacement vectors $\mathbf{U}^a$ and $\mathbf{U}^b$ have been obtained, the vector of slips/uplifts between the observed particles P^a and P^b can be derived as

$$\Delta\mathbf{R} = \mathbf{R}^b(x,z) - \mathbf{R}^a(x,z) = \mathbf{U}^b(x,z) - \mathbf{U}^a(x,z) \tag{27}$$

$$\Delta\mathbf{R} = \Delta^*(x,z)\mathbf{e}_t^*(x) + d^*(x,z)\mathbf{e}_n^*(x), \tag{28}$$

$$\Delta^*(x,z) = U_t^{b,*}(x,z) - U_t^{a,*}(x,z), \tag{29}$$

$$d^*(x,z) = U_n^{b,*}(x,z) - U_n^{a,*}(x,z). \tag{30}$$

Δ^* introduced in Eqs. (27)–(30) represents the 'mean' slip between the two initially coincident points in the tangential direction $\mathbf{e}_t^*(x)$; analogously, d^* is the 'mean' uplift in the direction $\mathbf{e}_n^*(x)$. The magnitudes of the contact tractions are assumed to depend on Δ^* and d^*:

$$\mathbf{p}_{cn}^{a,*} = -\mathbf{p}_{cn}^{b,*} = \begin{Bmatrix} p_{cn,t}^{a,*} \\ p_{cn,n}^{a,*} \end{Bmatrix} = \begin{Bmatrix} f(\Delta^*(x,z), d^*(x,z), T) \\ g(\Delta^*(x,z), d^*(x,z), T) \end{Bmatrix}. \tag{31}$$

In structural engineering applications, it often suffices to assume that the tangential contact traction depends essentially only on slip, while the normal contact traction depends only on uplift [24]. Then the contact law given in Eq. (31) may be largely simplified, resulting in

$$\mathbf{p}_{cn}^{a,*} = -\mathbf{p}_{cn}^{b,*} = \begin{Bmatrix} p_{cn,t}^{a,*} \\ p_{cn,n}^{a,*} \end{Bmatrix} \approx \begin{Bmatrix} F(\Delta^*(x,z), T) \\ G(d^*(x,z), T) \end{Bmatrix}. \tag{32}$$

Note that the actual mathematical form of the contact laws, described by the functions F and G, is to be determined by separate experiments for the actual type of the connection. After inserting Eq. (32) into Eqs. (16) and (17), we end up with

$$\begin{Bmatrix} \mathcal{P}_{cn,t}^{a,*} \\ \mathcal{P}_{cn,n}^{a,*} \\ \mathcal{M}_{cn,m}^{a,*} \end{Bmatrix} = \begin{Bmatrix} -\mathcal{P}_{cn,t}^{b,*} \\ -\mathcal{P}_{cn,n}^{b,*} \\ -\mathcal{M}_{cn,m}^{b,*} \end{Bmatrix} = \begin{Bmatrix} \int_s p_{cn,t}^{a,*}\,\mathrm{d}s \\ \int_s p_{cn,n}^{a,*}\,\mathrm{d}s \\ \int_s z\,p_{cn,t}^{a,*}\,\mathrm{d}s \end{Bmatrix} = \begin{Bmatrix} \mathcal{F}(\Delta^*(x,z), T) \\ \mathcal{G}(d^*(x,z), T) \\ \mathcal{H}(\Delta^*(x,z), T) \end{Bmatrix}. \tag{33}$$

In Eq. (33) $\int_s \ldots \mathrm{d}s$ refers to a line integral with respect to parameter s ($s = [0\ L_{\text{contact}}]$) along the contact line (Fig. 1). Prior to inserting the derived components of the contact traction vectors defined in Eq. (33) into Eqs. (11)–(13), these should be adequately transformed into the global coordinate basis.

The final system of equations of the proposed mechanical submodel is solved numerically applying the strain-based FE method as proposed in Kolšek et al. [1]. If, in any of the layers, its tangent constitutive matrix of the cross-section becomes zero, the cross-section is said to have reached its ultimate bearing capacity. Similarly, when the singularity of the global tangent stiffness matrix of the whole structure is reached in the course of the FEM analysis, the structural system is said to have reached its ultimate bearing capacity.

3. Verification of the model and numerical examples

In the following subsections, the present model will be applied to analyses of some practical examples of steel–RC composite beam-like structures. Firstly, the verification of the proposed model will be performed separately for the hygro-thermal and the mechanical part of the model.

Since some verifications of the adopted hygro-thermal submodels have been already carried out in [1,6], they will not be repeated here. In [1], the experiment of Khan [25], investigating a high temperature pore pressure build-up behaviour in the concrete wall of a reactor containment vessel, is numerically simulated and a good agreement between the experimental and numerical results is demonstrated. This problem appears to be rather simple because no mechanical load is applied prior to heating and negligible stresses only evolve in concrete due to thermally induced material dilatations. The permeability of concrete in such a case can be assumed to evolve as proposed in [9]. As already discussed in Section 2.2.2, the stresses induced in a composite structure prior and/or during fire should be accounted for in the permeability calculations. In a multi-step numerical model such as proposed in this study, this can only be achieved indirectly, using the empirically supported permeability model such as the one of Dwaikat and Kodur [6,12]. An experimentally supported validation of the submodel of Dwaikat and Kodur is presented in [6,12].

The verification of several aspects of the mechanical submodel, proposed by the present authors, has also been already made in their recent papers [3,1,21,22]. One of these aspects is, e.g. the question whether a planar Reissner's beam model is sufficiently accurate to simulate the behaviour of RC beams at high temperatures. Together

with the suitability of the suggested principle of additivity of strains and corresponding selected material models this was first demonstrated in [21] where the results for the fire-exposed centrically loaded RC column are compared against experimental results of Lin et al. [26]. Later on, the suitability of these principles was additionally demonstrated on a case of a plain steel beam discussing two suggested submodels for high-temperature mechanical and creep strains of steel, i.e. [18] and [19]. In [3] the suitability of the Reissner's model and of the employed principle of additivity of strains was shown once more, this time for the steel–concrete composite beam with flexible tangential interlayer connection. The numerical results were here compared against experimental data of Wainman and Kirby [27].

In the present study, the validation of the present improved mechanical model accounting for both tangential and normal flexibility of the contact will be carried out on the composite plate of Guo and Bailey [28]. Unfortunately, in the experiments performed by Guo and Bailey [28] slips and uplifts were not measured, in fact – to the authors' knowledge – they have not been observed elsewhere; thus no fully experimentally supported comparison of this fundamentally novel aspect of the present improved model could be displayed. Instead, the verification of the proposed contact submodel is made by comparing the present numerical results with the corresponding numerical results of a 3D solid model set in the commercial FEMA software LUSAS.

In Section 3.2 the verification of the model is followed by a demonstration of the present model's practical application. The response of a trapezoidal RC plate strengthened externally with a thin steel sheet and subject to fire is shown, applying different amount of the tensile reinforcement placed in each rib of the RC deck, and different tangential and normal contact stiffness of the interlayer connection.

We find it convenient for the reader to collect some basic assumptions made in the examples to follow. Since these meet the assumptions already gathered in [1] (see the preliminary part of Section 3 of [1]) they will not be repeated in this paper. It must be pointed out, however, that, in contrast to [1], the connection between the steel and the RC layer in the hygro-thermal analysis is, in the present paper, not considered to be perfect during fire, since an interlayer uplift is assumed to evolve. In addition, two constitutive laws of steel [19] are adopted in the present study, i.e. material laws [19] and [18].

3.1. Verification of the proposed model

3.1.1. The composite plate of Guo and Bailey

Our first numerical example is the RC plate combined with a thin trapezoidal steel sheet subjected to 16-point loading. The plate was analysed experimentally by Guo and Bailey [28]. Their results are used for the validation of the mechanical part of the present numerical model.

In setting the numerical model of the plate, we assume a purely planar bending of the plate, so that it can be modelled as a three-span beam (see Fig. 2a and b) subject to a 4-point loading P and some specified fire conditions (Fig. 2c). The cross-section of the beam is taken to be equal to the cross-section of one rib (Fig. 2b). Two of the Guo and Bailey's examples [28] are analysed. We denote them by GB-1 and GB-2. In the first example (plate GB-1), the load magnitude is $P=4.5$ kN. In the second example (plate GB-2), we assume $P=2.75$ kN.

The material characteristics of the RC deck and the steel sheet at room temperature as reported in Guo in Bailey [28] and also adopted in the present numerical analysis are as follows: the yield strength of steel of the trapezoidal sheet is $f_{y,20}=37.8$ kN/cm^2, the yield strength of steel of the reinforcing bars is $f^r_{y,20}=65$ kN/cm^2, and the strength of concrete $f_{c,20}$ for cases GB-1 and GB-2, respectively, is

3.8 kN/cm^2 and 4.0 kN/cm^2. The rest of material data at room temperature, not provided in [28] but essential for the analysis, are selected as follows: the elastic modulus of steel of the trapezoidal sheet is $E_{s,20}=2.1 \times 10^4$ kN/cm^2, the elastic modulus of steel of the reinforcing bars is $E^r_{s,20}=2.1 \times 10^4$ kN/cm^2, and the secant elastic modulus of concrete is $E_{c,20}=3.1 \times 10^3$ kN/cm^2. The material law of steel at elevated temperatures is taken to be bilinear for steel along with the corresponding reduction coefficients in terms of [19].

Note that, as also reported in [22], the phenomenon of creep in steel is not included in this material model. Therefore, we have to include creep of steel explicitly, here using the model of Williams-Leir [29] for steel class Austen 135. For capturing essential material phenomena in concrete at elevated temperature, we follow Bratina et al. [21] and adopt the material constitutive laws presented in [15,30,31]. Furthermore, Guo's law [4] for the room temperature law of contact for the tangential direction is assumed in the analysis (Fig. 2d). Since in [4] no indication is given on how this contact law should be modified for elevated temperatures, we introduce only a very simple assumption that the maximum strength of the contact is reduced by factor A given in Table 1. A good agreement between experimental and numerical results, presented in the subsections to follow, shows this one to be a reasonable assumption. In addition, no information is given in [4] regarding the contact law in the normal direction. Yet, in terms of the magnitude error in the plate midspan deflection, observed in the present example, this is found to be irrelevant.

Our analysis starts with the determination of the time- and space-dependent temperature field in the plate area $\overline{T_3T_5}$ (see Fig. 2a). The pore pressures, which could evolve along the contact between the steel sheet and the concrete plate during fire, are in the present analysis taken as negligible. This assumption is plausible because the steel and the RC layer soon separate from each other during the deformation. In addition, the concrete zone around the contact is, in these types of structures, in tension initially and, therefore, damaged. Thus, a substantial increase of the concrete permeability is expected to evolve in this area. Moreover, due to its low thickness and due to a high thermal conductivity of steel, the trapezoidal sheet represents a negligible thermal protection of the RC deck. Thus, it can be assumed that the temperature of the steel sheet is approximately constant across its thickness and nearly equal to the temperature of the lower surface of the RC plate. In view of the above assumptions, only the RC part of the cross-section is treated in the hygro-thermal analysis neglecting the thermal effects of the steel sheet. See Fig. 2b for the details of the corresponding hygro-thermal boundary conditions.

In Guo and Bailey [28], no information on the hygro-thermal properties of concrete, being crucial in heat and mass transfer analyses of concrete structures, is given explicitly. Thanks to their remark that a normal strength concrete was used in the experiments, the following hygro-thermal data can be estimated: initial content of water vapour in air within the concrete pores $\tilde{\rho}_{V,0}=0.0111$ kg/m^3 ($RH^0=60\%$), air water vapour content at the boundary $\tilde{\rho}_{V,\infty}=0.0074$ kg/m^3 ($RH^0=40\%$), free water content at full saturation of air inside concrete pores and at ambient temperature $\overline{\rho}^{sat}_{FW,0}=90$ kg/m^3, initial porosity of concrete $p^0_{or}=0.12$, and initial concrete permeability $K_0=3 \times 10^{-15}$ m^2.

A comparison between the measured and the simulated development of temperatures in time is shown in Fig. 3a and b. The variations of temperatures at the measuring positions T15, T16, T19, and T20, T21, T22 are displayed (the positions of the embedded thermocouples are shown in Fig. 2b). The agreement between the results is generally good, although some significant discrepancies can be observed at positions T19 and T22 (these are the positions close to the heated surface). At the positions T19 and T22, the experimentally and numerically defined graphs of Fig. 3a
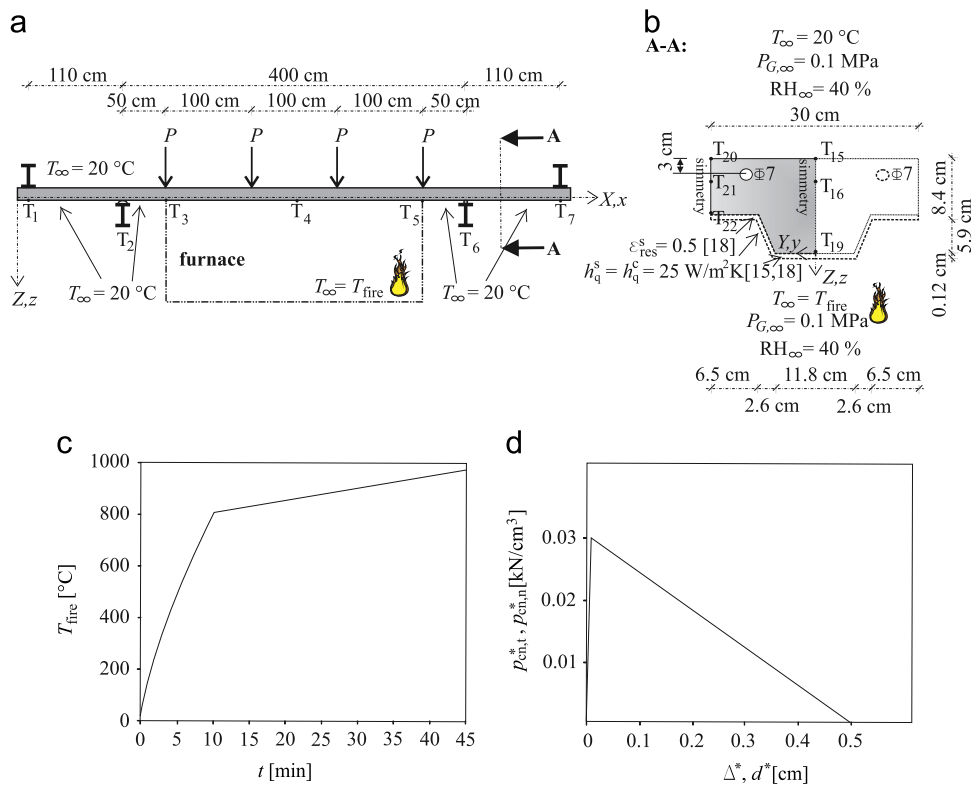
Fig. 2. Composite plate of Guo and Bailey. (a) Test assembly. (b) Cross-section of the beam model with displayed hygro-thermal boundary conditions. (c) Fire scenario. (d) Slip/uplift vs. corresponding magnitude of the shear contact surface force at ambient temperature. The denotations T_∞, h_c^q, h_s^q, and ϵ_s^{res}, respectively, apply to the temperature of the surrounding compartment, the convection coefficients at the concrete and the steel surface of the structure, and the emissivity of the steel surface as they were accounted for in the calculations of thermal flow boundary conditions.

Table 1
Proposed values of parameter A for elevated temperatures.

T (°C)	≤ 100	200	300	400	500	600	700	≥ 800
A	1	1	0.9063	0.8567	0.5909	0.3911	0.1964	0.1472

and b match approximately up to 5 min of the observed time. The curves at the position T21 match much better – the differences start growing after 20 min, but remain small. Recall that, in the hygro-thermal numerical model employed in this paper, the thermal parameters of concrete from EC2 [15] are used (see the corresponding assumption of the model in Section 2.2.2). These correspond well to moist concrete only and, therefore, are appropriate for the proposed model only as long as the concrete pores are at least partially filled with water. The observed deviations of the results for the positions T19, T21, and T22 are, thus, most likely due to the absence of free water around these positions. Fig. 3d confirms this speculation revealing that the area around the positions T19 and T22 appears in the numerical simulation to become completely dry after 10 min of the fire already. For the position T21 the same is observed after 20 min have elapsed.

In the mechanical subanalysis, two magnitudes of the four-point loading, i.e. $P=4.5$ kN (plate GB-1) and $P=2.75$ kN (plate GB-2), are observed. The comparison between the experimental and numerical results for the time-dependent midspan deflection for the two cases is shown in Fig. 4. Prior to the temperature of the steel sheet reaches 500 °C, which occurs at around 15 min of fire, see Fig. 3c, a good agreement between the experimental and numerical results can be observed for both load levels. For the lower load level, a good agreement is also observed throughout the rest of the time of the fire. However, somewhat higher and increasing discrepancies are observed for the higher load level. Given that temperature-dependent properties

of steel of [19] were used, such results are expected. Namely, and as reported in [22], the relevant data in [19] are only valid for lower load levels. Some discrepancy may likely to occur due to the neglected transversal shear capacity of the plate, which cannot be considered by the present beam model.

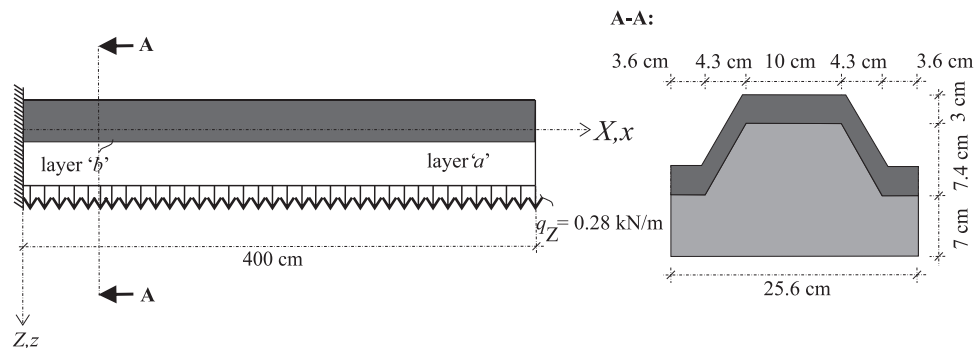### 3.1.2. Externally strengthened elastic cantilever beam at ambient conditions

The goal of the present example is a further validation of the mechanical submodel, presented in Section 2.2.3. This example is focused on the validity of the proposed contact submodel. We investigate a two-layered composite cantilever beam shown in Fig. 5. For simplicity both layers are taken to be made of elastic homogeneous materials and subject to a constant uniformly distributed traction $q_Z=0.28$ kN/m at ambient temperature. The elastic modulus of layer 'a' is $E_{c,20}^a = 3.1 \times 10^3$ kN/cm^2; the elastic modulus of layer 'b' is $E_{s,20}^b = 2.1 \times 10^4$ kN/cm^2. The interlayer connection is also taken to behave linearly having the stiffnesses $k_X = k_Z = 0.25$ kN/cm^3, so that $p_{cn,t}^{a,*} = 0.25\Delta^*$ and $p_{cn,t}^{a,*} = 0.25d^*$. The ultimate material and contact strengths are taken to be unbounded. Furthermore, both layers are fixed at the left end and free at the right. In the mechanical analysis, two separate numerical models are engaged, i.e. the present 1D beam model, proposed in Section 2, and a 3D solid numerical model set in the LUSAS finite element analysis software. There the layers are modelled by the HX9M finite elements (LUSAS 3D isoparametric solid FEs) and the connection between the layers is modelled using the JNT4 FEs (LUSAS 3D joint FEs connecting two nodes by three springs in the local x, y, and z directions). A comparison between the results for displacements and internal forces of the two models is shown in Table 2. The results are in an excellent agreement. This completes the validation of the proposed model
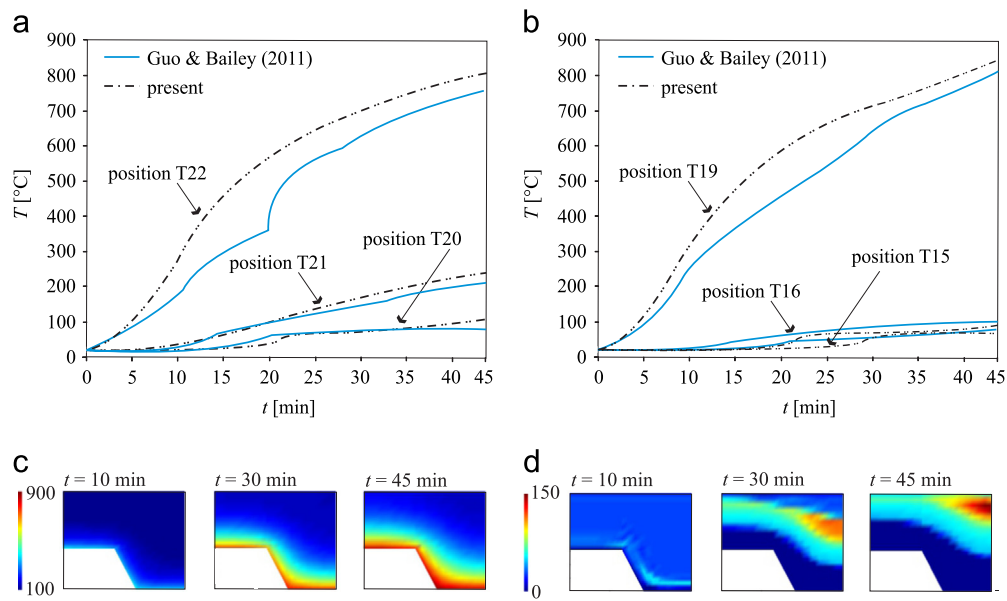
Fig. 3. Composite plate of Guo and Bailey [28]. Time evolution of temperatures at positions of embedded thermocouples (a) T20, T21, T22 and (b) T15, T16, T19. Cross-sectional distribution of (c) temperature and (d) free water content.
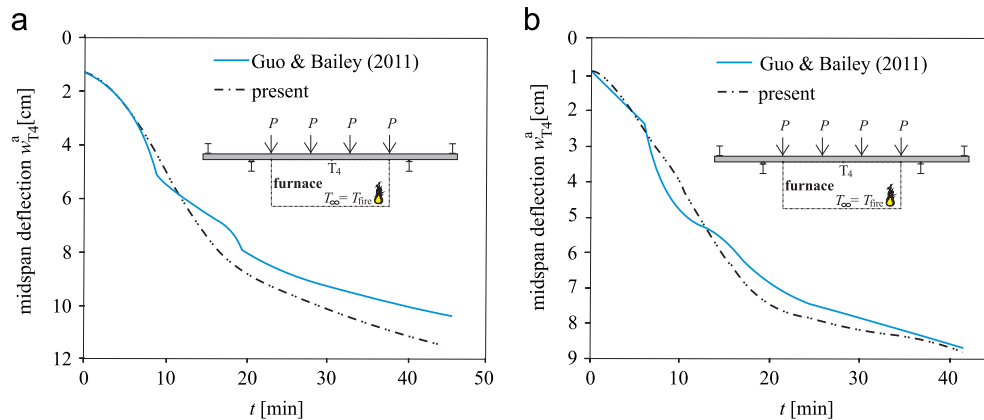
Fig. 4. Composite plate of Guo and Bailey [28]. Time–deflection curves for two levels of mechanical point loading.

Fig. 5. Externally strengthened elastic cantilever beam at ambient temperature. Geometric characteristics.

and confirms the suitability, accuracy, and numerical efficiency of the proposed 1D numerical model.

3.2. Parametric study of fire resistance of steel–RC trapezoidal composite plate

In the parametric study to follow we investigate the effect of the tensile reinforcement and the contact stiffness on the fire resistance of a simply supported steel–RC trapezoidal composite plate exposed to ISO 834 [14] fire conditions. A typical rib of the slab, shown in Fig. 6a and b, is analysed by the present beam model. In addition to the steel trapezoidal sheet, a tensile reinforcement bar is placed in each rib of the RC deck. In Fig. 6b the number of the bars per rib is denoted by n and the diameter of an individual bar is marked by ϕ^{r}.

In the hygro-thermal step of the fire analysis, the same assumptions are adopted for consideration of heat and mass transfer as in Section 3.1.1; thus, only the concrete part of the cross-section is

modelled. The hygro-thermal properties of a standard normal strength concrete are chosen as in Section 3.1.1. Results of the analysis for the cross-sectional temperature fields at various times are shown in Fig. 6c. The predicted temperature fields are used as the input data for the final, mechanical step of the fire analysis.

The material data at room temperature are taken as follows: the yield strength of steel of the trapezoidal sheet is $f_{y,20} = 28$ kN/cm^2, the compressive strength of the concrete is $f_{c,20} = 3$ kN/cm^2, and the yield strength of steel of the rebars is $f_{y,20}^r = 40$ kN/cm^2. The high-temperature stress–strain law for steel follows EC3 [18]. This one is to be contrasted to the material model of steel offered in [19] and also employed in Section 3.1.1, where creep of steel is considered explicitly. Note that in the EC3 material model, the creep strain in steel is integrated within the plastic strain. Thus creep should not be treated in an additive manner in this example. The stress–strain relationship for concrete with siliceous aggregates is chosen in the present paper and the corresponding data are taken from EC2 [15]. Following the recommendations of Bratina et al. [21] the effects of creep and transient strains in concrete are treated explicitly, see [30,31]. The contact constitutive law at room temperature is selected as

$$p_{cn,t}^{a,*}(x,z) = A\tau_{cn,t,20,max}(1 - e^{-B\Delta^*}), \qquad (34)$$

$$p_{cn,n}^{a,*}(x,z) = A\tau_{cn,n,20,max}(1 - e^{-Bd^*}), \qquad (35)$$

with $\tau_{cn,t,20,max}$ and $\tau_{cn,n,20,max}$ denoting the tangential and the normal ultimate strength of the contact at room temperature, respectively.

These strengths will be in the upcoming subsections chosen as suitable parameters in parametric analyses. Observe that the mathematical description of the contact law in Eqs. (34) and (35) is chosen with an aim to getting eloquent and vivid conclusions of the presented parametric study. The selected law is similar but not identical to that of Huang et al. [32]. Nevertheless, the proposal seems to represent realistic situations well. The values of parameters A and B from Eqs. (34) and (35) are presented in [32].

In what follows, two parametric studies are performed considering (i) different ratios of tensile reinforcement and (ii) different contact stiffnesses.

3.2.1. Influence of tensile reinforcement ratio

We first study the effect of the ratio of the tensile reinforcement on the fire response of the slab. The tensile reinforcement ratio is in this paper defined as the ratio between the cross-sectional area of the rebars, installed within the ribs of the trapezoidal RC deck, and the cross-sectional area of the compositely attached steel sheet. Three different cases will be studied: (i) case S1–O with two rebars of diameter $\phi^r = 14$ mm per rib and the tensile reinforcement ratio 1.06, (ii) case S2–O with two rebars $\phi^r = 10$ mm per rib and the corresponding tensile reinforcement ratio 0.54, and (iii) case S3–O with one rebar $\phi^r = 8$ mm per rib and the tensile reinforcement ratio 0.17. The results of the three composite slabs will also be compared with the results of cases S1–N, S2–N, and S3–N representing the plain RC slabs, having the

Table 2
Elastic two-layered cantilever beam at ambient conditions. A comparison between numerical results of (A) the 3D solid LUSAS FEM numerical model and (B) the present numerical model.

x (cm)	$u^a - u^b$ (10^{-2} mm)		$w^a - w^b$ (10^{-2} mm)		N^a (kN)		N^b (kN)		Q^a (kN)		Q^b (kN)	
	(A)	(B)	(A)	(B)	(A)	(B)	(A)	(B)	(A)	(B)	(A)	(B)
0	0	0	0	0	−11.4	−11.3	11.4	11.3	−1.1	−1.1	−1.1	−1.1
50	1.8	1.8	1.2	1.2	−10.9	−10.8	10.9	10.8	−0.8	−0.8	−1.1	−1.1
100	3.0	2.9	2.9	2.9	−9.8	−9.7	9.8	9.7	−0.6	−0.6	−1.0	−1.0
150	3.6	3.5	3.9	3.9	−8.2	−8.1	8.2	8.1	−0.5	−0.5	−0.9	−0.9
200	3.8	3.7	4.3	4.3	−6.5	−6.4	6.5	6.4	−0.4	−0.4	−0.7	−0.7
250	3.8	3.7	4.3	4.3	−4.8	−4.7	4.8	4.7	−0.4	−0.4	−0.5	−0.5
300	3.6	3.6	3.9	3.9	−3.1	−3.1	3.1	3.1	−0.3	−0.3	−0.3	−0.3
350	3.4	3.4	3.1	3.1	−1.5	−1.5	1.5	1.5	−0.2	−0.2	−0.1	−0.1
400	3.3	3.3	1.9	1.9	0	0	0	0	0	0	0	0
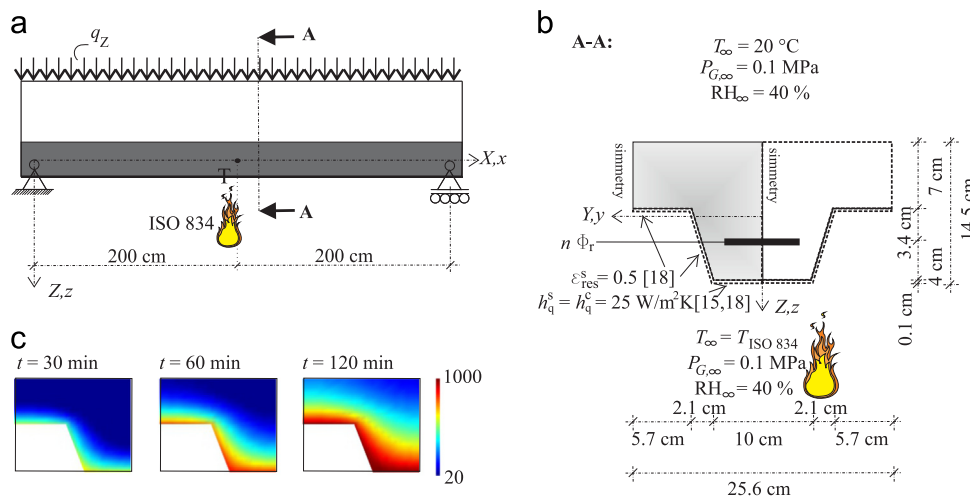
Fig. 6. Parametric study of a simply supported composite RC plate with trapezoidal steel sheet. (a) Geometric characteristics of the problem. (b) Cross-section and boundary conditions for the hygro-thermal part of the analysis. (c) Distribution of temperatures over the concrete part of the cross-section at chosen times. The denotations T_∞, h_q^g, h_s^g, and ϵ_s^{res}, respectively, apply to the temperature of the surrounding compartment, the convection coefficients at the concrete and the steel surface of the structure, and the emissivity of the steel surface as they were accounted for in the calculations of thermal flow boundary conditions.

same geometric, material, and loading characteristics as the plates S1–O, S2–O, and S3–O, yet with no external tensile reinforcement (i.e. having no steel sheet). The following loading data are employed. In case S1 each rib of the RC slab is subjected to traction $q_Z = 4.62$ kN/m, distributed uniformly along the whole length of the rib. In cases S2 and S3, the tractions are $q_Z = 2.57$ kN/m and 0.86 kN/m, respectively. In any of the three cases, the selected loads represent approximately 90% of the elastic bearing capacity of the corresponding plain RC slabs S1–N, S2–N, or S3–N. Note that the self-weight of the slab is included in the given load magnitudes.

Fig. 7 shows the evolution of the midspan deflection for cases S1–O, S1–N, S2–O, S2–N, S3–O, and S3–N. The comparison between the graphs for cases S1–O and S1–N, when the tensile reinforcement ratio is high, shows that the fire resistances of the RC deck with and without steel sheet are similar. About 8 min bigger fire resistance of plate S2–O is observed compared to S2–N. Very different fire resistances are experienced in slabs S3–O with the minimal tensile reinforcement ratio and S3–N. As high as half an hour difference in the final fire resistances is estimated. The rational explanation for such an observation is given below.

The transition between the approximately linear part of the load–deflection curves, see Fig. 7, and the highly non-linear steep part of the curves occurs when the first point of the steel sheet reaches the yielding state. Once the transition point is passed, the yielding zone gradually extends from the exposed bottom towards the upper edge of the steel sheet cross-section, and only after a substantial part of the cross-section of the steel sheet has yielded, the reinforcing bars start yielding, too. The midspan deflection of the slab suddenly increases and continues to grow rapidly at a nearly constant
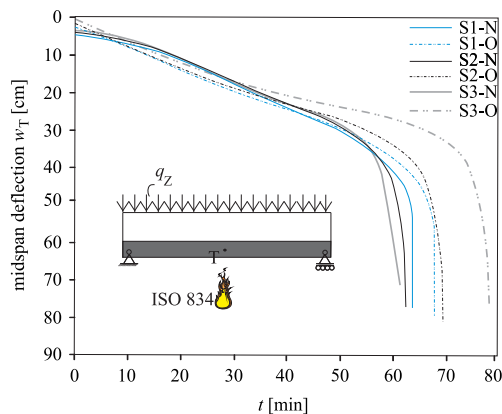

Fig. 7. The effect of the tensile reinforcement ratio. Development of the midspan deflection over time.

temperature (observe the almost vertical segments of the graphs in Fig. 7). It is obvious that the failure of the composite slab largely depends on the time the rebars start to yield.

The time also depends on how big a portion of the overall tensile stress induced in the plate is overtaken by the rebars. In the cross-section of a steel–RC composite plate, the distribution of the tensile stress between the rebars and the steel sheet mainly depends on the ratio of their rigidities. If the concrete part of the cross-section is reinforced stronger (such as in cases S1 and S2), then the tensile stress is mainly equilibrated by the reinforcing bars and, therefore, the RC slab does not rely much on the steel sheet. This is expected to be so, since the contribution of the steel sheet to the tensile bearing capacity of the composite plate is with time even smaller because the steel sheet temperatures are always higher than the temperatures of the steel rebars. A different conclusion, however, can be drawn for case S3. In this case the cross-sectional area of the rebars is minimal. Consequently, most of the tensile stress is taken by the steel sheet, yet this does not change significantly even if the temperature in the sheet gets substantially higher.

3.2.2. Influence of tangential and normal contact stiffness

We now focus on the influence of the interlayer contact stiffness on the fire resistance of the composite plate. Plate S2–O is only observed and the effects of different values of contact stiffness are investigated. The influence of tangential contact stiffness $\tau_{cn,t,20,max}$ is first analysed. The initial value of $\tau_{cn,t,20,max}$ is set to 0.59 kN/cm. This value is then largely increased to model a rigid contact (S2–Oa), then further reduced firstly to one-half (S2–Ob) and then to one-fifth of the initial value (S2–Oc). In the normal direction, the contact stiffness remains constant: $\tau_{cn,n,20,max} = 0.59$ kN/cm.

The time–midspan deflection curves are shown in Fig. 8a. The numerical results show that large slips evolve between the steel sheet and the RC layer for cases S2–Oa and S2–Ob. Nevertheless, as long as the failure of the contact does not take place prior to instability of at least one of the concrete or steel cross-sections, or the global structural instability occurs, such a contact stiffness reduction seems to have a very small impact on the evolution of the deflections. Observe that the curves for S2–O, S2–Oa, and S2–Ob in Fig. 8a almost coincide.

Different conclusions can be, however, made for the case where the contact is highly flexible, such as in case S2–Oc. Then slips between the steel and the RC layer become critical at about 14 min of fire, when the tangential contact starts failing. It is reasonable to assume that the failure of the contact in the tangential direction triggers the normal contact failure also (in a form of an uplift), and vice versa. A closer look into the results of the numerical analysis of case S2–Oc shows that the failure of the contact starts in the vicinity
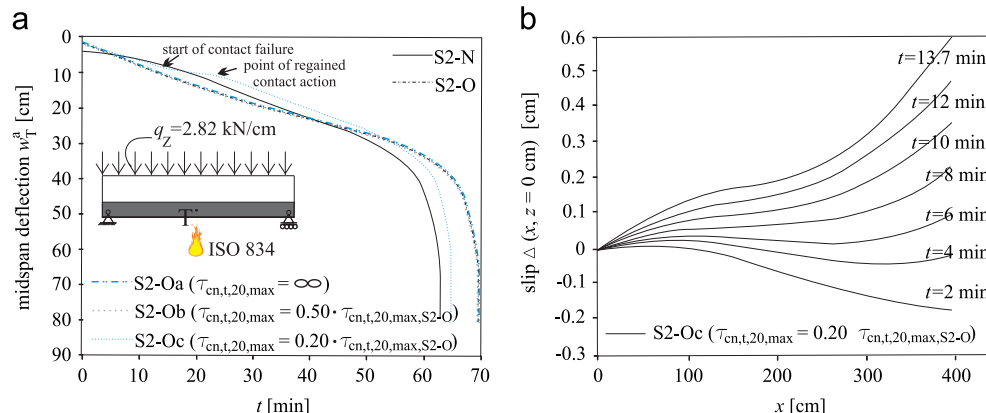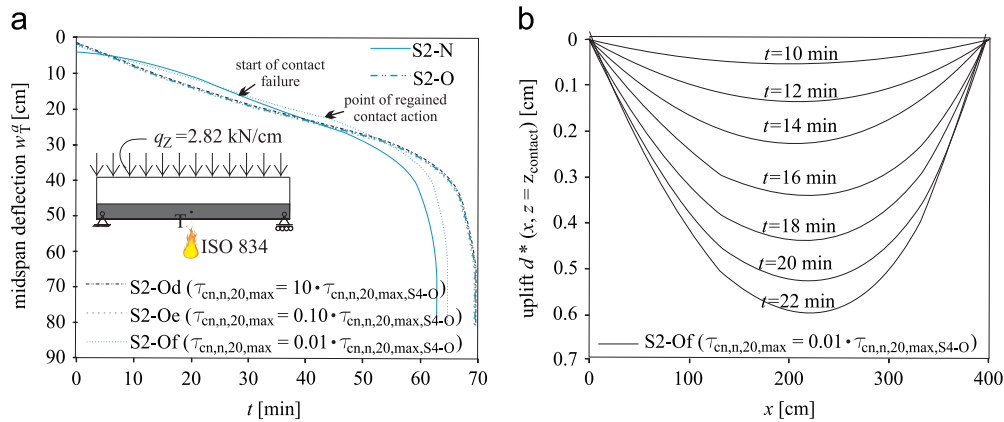

Fig. 8. Parametric study on the influence of the tangential contact stiffness on fire resistance. (a) Time evolution of the midspan deflection. (b) Time evolution of interlayer slip over the length of the beam for plate S2–Oc.

Fig. 9. Parametric study on the influence of the normal contact stiffness on fire resistance. (a) Time evolution of the midspan deflection. (b) Time evolution of interlayer uplift over the length of the beam for case S2–Of.

of the roller support of the beam, and subsequently, within only a few minutes, expands over the whole contact surface. Note that this is truly a fast redistribution of the contact loading. After complete debonding of the contact area has occurred, the separated steel layer remains to rest on the plate supports for few short moments. After some time the RC deck again approaches the sheet, eventually leaning itself on it. At this instant the transverse part of the contact action is fully recovered. Thus some contribution (although substantially smaller compared to cases S2–O, S2–Oa, and S2–Ob) of the sheet to the fire response of the structure is regained. This is clearly seen from the non-coinciding, yet parallel graphs of S2–O and S2–Oc for the time domain of the regained contact, i.e. 20 min $\leq t \leq 70$ min in Fig. 8a. Observe also the corresponding difference between their ultimate fire resistances.

Within the time domain $t \geq 14$ min, the midspan deflection in plate S2–Oc is less than the midspan deflection in the corresponding plain RC plate (S2–N). This appears to be due to an early failure of the interlayer connection, observed at about 14 min of fire. The contact failure has a beneficial effect on the overall slab behaviour, because the thermal expansion of the steel sheet has no longer a large effect on the concrete deck.

In Fig. 9 we show the effect of the stiffness of the normal contact connection. In investigating this effect, the tangential stiffness of the contact is assumed as being fixed at $\tau_{cn,t,20,max} = 0.59$ kN/cm, while in the normal direction, the contact stiffness is varied from $\tau_{cn,n,max} = 0.59$ kN/cm (case S2–Od) followed by a 10 times higher (case S2–Oe), a 10 times lower (case S2–Of), and, finally, by a 100 times lower normal contact stiffness (case S2–Og). The results for the midspan deflection are displayed in Fig. 9a. Similar conclusions can be drawn as in the previous study that the normal contact stiffness has only a small effect both on the deflection and on the ultimate structural fire resistance, if it is sufficiently stiff (cases S2–Od, S2–Oe, and S2–Of). If, by contrast, a too flexible normal contact connection (like in case S2–Og) is designed, such that the contact fails prior to the bearing capacity of the RC deck is attained, a substantial reduction of the fire resistance time occurs.

For a better illustration, slips and uplifts evolving between the layers of the plate with the most flexible normal interlayer connection, plates S2–Oc and S2–Of, respectively, are shown in Figs. 8b and 9b.

4. Conclusions

In this paper a new fully generalised numerical model has been proposed and validated for the performance-based fire analysis of steel–RC composite beam-like structures. The model is generalised in the sense of employing submodels for all physical phenomena and their couplings that are at date recognised as potentially

influential on the fire response of composite structures. The model accounts for (i) geometrical and material non-linearity, (ii) an arbitrary contact connection with possible tangential and normal slips and uplifts, (iii) moisture in concrete and the corresponding physical and chemical phenomena (mass transfer of water vapour, dry air, and free water, evaporation, condensation, dehydration etc.), (iv) a thermal and mechanical damage in concrete, and (v) material related high temperature phenomena (material hardening/softening, creep etc.). Although some of the adopted material constitutive submodels (especially those of hygro-thermal response of concrete and concrete spalling) are still a matter of ongoing research and validation studies, the model can be at date of a use to a broader fire research community for performing parametric studies. These can explore importance of specific physical phenomena for efficiency and accuracy of the discussed performance-based simulations and detect those of them that can or cannot be neglected in the model or accounted for in a simplified manner. Thereby, the model can provide good directions for further research. An example of such a study was also presented in the final part of the paper showing parametric investigations of the contribution of the thin steel sheet and of the stiffness of the steel sheet–RC contact connection to the overall structural fire resistance of standard trapezoidal steel–RC floor slabs. Lacking suitable experimental data from the available literature, in these studies different values of the contact stiffness were discussed in the range assumed to be plausible. The results showed that a high contribution of the steel sheet can be only expected when the ratio between the tensile stiffness of the reinforcing bars and the tensile stiffness of the trapezoidal sheet is low; e.g. for the ratio 0.17, a more than 30% increase in the ultimate fire resistance time of the plate has been discovered. Furthermore, the investigation of the effect of the tangential and normal interlayer contact stiffness has shown the important feature of the stiffness that when the contact does not fail prior to the cross-sectional or global structural instability has been reached, the contact stiffness has practically no influence on the shape and the magnitude of the time–deflection curve nor it influences its ultimate fire resistance time. By contrast, when the contact stiffness is so small that the contact fails very early, the contribution of the steel sheet to the structural fire resistance is reduced substantially. In addition, the failure of contact has been found to evolve very fast and with an ability to develop fully even prior to warningly high deflections of the plate evolve. For specific cases of composite structures, where boundaries of the steel layer are not supported and where the overheated steel layer may peel off during fire, the contact failure could, therefore, represent a threat from the point of view of evacuation and rescue. Along with

these conclusions, the presented parametric study also (i) showed that, in the calculations of the structural fire response, the inclusion of the influence of the thin steel sheet layers can be important for some cases of steel–RC composite beam-like structures and, consequently, (ii) pointed out the need for developing new experimentally supported models of high-temperature response of steel sheet–RC beam interlayer interactions of such structures.

Acknowledgement

References

[1] J. Kolšek, I. Planinc, M. Saje, T. Hozjan, The fire analysis of a steel–concrete side-plated beam, Finite Elem. Anal. Des. 74 (2013) 93–110.

[2] S. Foster, M. Chladna, C. Hsieh, I. Burgess, R. Plank, Thermal and structural behaviour of a full-scale composite building subject to a severe compartment fire, Fire Saf. J. 42 (2007) 183–199.

[3] T. Hozjan, M. Saje, S. Srpčič, I. Planinc, Fire analysis of steel–concrete composite beam with interlayer slip, Comput. Struct. 89 (2011) 189–200.

[4] S. Guo, Experimental and numerical study on restrained composite slab during heating and cooling, J. Constr. Steel Res. 69 (2012) 95–105.

[5] J. Kolšek, T. Hozjan, M. Saje, I. Planinc, Analytical solution of linear elastic beams cracked in flexure and strengthened with side plates, J. Compos. Mater. 47 (2013) 2847–2864.

[6] M.B. Dwaikat, V.K.R. Kodur, Fire induced spalling in high strength concrete beams, Fire Technol. 46 (2010) 251–274.

[7] D. Gawin, F. Pesavento, B.A. Schrefler, Towards prediction of the thermal spalling risk through a multi-phase porous media model of concrete, Comput. Methods Appl. Mech. Eng. 195 (2006) 5707–5729.

[8] H. Zhang, C. Davie, A numerical investigation of the influence of pore pressures and thermally induced stresses for spalling of concrete exposed to elevated temperatures, Fire Saf. J. 59 (2013) 102–110.

[9] R. Tenchev, J. Purkiss, L. Li, Finite element analysis of coupled heat and moisture transfer in concrete subjected to fire, Numer. Heat Trans. Part A: Appl. 39 (2001) 685–710.

[10] Y. Ichikawa, G. England, Prediction of moisture migration and pore pressure build-up in concrete at high temperatures, Nucl. Eng. Des. 228 (2004) 245–259.

[11] C. Davie, C. Pearce, N. Bićanić, Coupled heat and moisture transport in concrete at elevated temperatures-effects of capillary pressure and adsorbed water, Numer. Heat Trans. Part A: Appl. 49 (2006) 733–763.

[12] M.B. Dwaikat, V.K.R. Kodur, Hydrothermal model for predicting fire-induced spalling in concrete structural systems, Fire Saf. J. 44 (2009) 425–434.

[13] A. Kroflič, M. Saje, I. Planinc, Non-linear analysis of two-layer beams with interlayer slip and uplift, Comput. Struct. 89 (2011) 2414–2424.

[14] ISO-834. Fire Resistance Tests—Elements of Building Construction, International Standard Organization, Geneva, 1975.

[15] Eurocode 2, Design of Concrete Structures, Part 1.2: Structural Fire Design, European Committee for Standardization, 2004.

[16] Z. Bažant, M. Kaplan, Concrete at High Temperatures: Material Properties and Mathematical Models, Longman, Harlow, 1996.

[17] E. Reissner, On one-dimensional finite-strain beam theory: the plane problem, J. Appl. Math. Phys. 23 (1972) 795–804.

[18] Eurocode 3, Design of Steel Structures, Part 1.2: Structural Fire Design, European Committee for Standardization, 2004.

[19] Construction métallique, Méthode de prévision par le calcul du comportement au feu des structures en acier, Document technique unifié, 1976.

[20] J. Simo, T. Hughes, Computational Inelasticity, Springer, New York, 1998.

[21] S. Bratina, B. Čas, M. Saje, I. Planinc, Numerical modelling of behaviour of reinforced concrete columns in fire and comparison with Eurocode 2, Int. J. Solid. Struct. 42 (2005) 5715–5733.

[22] T. Hozjan, G. Turk, S. Srpčič, Fire analysis of steel frames with the use of artificial neural networks, J. Constr. Steel Res. 63 (2007) 1396–1403.

[23] M. Bradford, R. Gilbert, Composite beams with partial interaction under sustained loads, J. Struct. Eng. 118 (1992) 1871–1883.

[24] A. Adekola, Partial interaction between elastically connected elements of a composite beam, Int. J. Solid. Struct. 4 (1986) 1125–1135.

[25] S.A. Khan, Pore pressure and moisture migration in concrete at high and non-uniform temperatures (Ph.D. thesis), King's College, University of London, 1990.

[26] T. Lin, R. Zwiers, R. Burg, T. Lie, R. McGrath, Fire Resistance of Reinforced Concrete Columns, PCA Research and Development Bulletin, RD101B, 1992.

[27] D. Wainman, B. Kirby, Compendium of UK Standard Fire Test Data, Unprotected Structural Steel - 1. Ref. No. RS/RSC/S10328/1/87/B, Swinden Laboratories, British Steel Corporation, Rotherham, UK, 1988.

[28] S. Guo, C. Bailey, Experimental behaviour of composite slabs during the heating and cooling fire stages, Eng. Struct. 33 (2011) 563–571.

[29] G. Williams-Leir, Creep of structural steel in fire: analytical expressions, Fire Mater. 7 (1983) 73–78.

[30] T. Harmathy, Fire Safety Design and Concrete, Longman, London, 1993.

[31] L. Li, J. Purkiss, Stress strain constitutive equations of concrete material at elevated temperatures, Fire Saf. J. 40 (2005) 669–686.

[32] Z. Huang, I. Burgess, R. Plank, The influence of shear connectors on the behaviour of composite steel-framed buildings in fire, J. Constr. Steel Res. 51 (1999) 219–237.